

Charging ain't all bad: Complex physics in DyScO₃

Christopher A. Mizzi, Pratik Koirala, Ahmet Gulec, Laurence D. Marks*

Department of Materials Science and Engineering, Northwestern University, Evanston, IL 60208, USA



ARTICLE INFO

Keywords:

Charging
Flexoelectricity
Surface states
EELS
DFT
UPS

ABSTRACT

Although charging is ubiquitous in electron microscopy, its effects are typically avoided or ignored. However, avoiding charging is not possible in some materials, e.g. lanthanide scandates with well-ordered surfaces positively charge immensely under electron beam illumination because of their electronic structure, and ignoring charging can leave new science undiscovered. In this work, a combination of rapidly acquired electron energy loss spectra and cross-correlation were used to understand and overcome charging effects in DyScO₃. A 5.4 eV band gap was extracted from the charging-corrected loss spectrum, in good agreement with previously reported band gaps, and a 3.8 eV in-gap peak was attributed to surface states via comparison with density functional theory calculations. Additionally, ultraviolet photoelectron spectroscopy measurements indicated that under some conditions well-annealed DyScO₃ surfaces charge negatively causing upward band bending associated with occupied surface states in the gap. As was previously found in the case of positive charging under electron beam illumination with in-situ flexoelectric bending observations, the magnitude of negative charging under ultraviolet illumination is Zener tunneling limited in well-annealed DyScO₃.

1. Introduction

Charging is one of the banes of electron microscopy. It impacts nearly all insulators and can be net positive or negative depending on the material, sample, and microscope conditions [1]. Given this ubiquity, there are a number of papers that detail charging effects in electron microscopy, e.g. [2–11]. In practice, electron microscopists typically treat charging as a nuisance to be avoided at all costs, resorting to processing the sample (e.g. depositing carbon passivating films) or some other approach to avoid charging effects. A particular case where charging is prevalent is electron cryomicroscopy [12,13] because thin films of ice [14] and amorphous carbon supports at liquid nitrogen temperatures [15] are poor conductors.

Sample charging is not always the nuisance it is made out to be, but instead can be a source of new phenomena. One example is the observation of abnormally large bending in lanthanide scandates [16], a phenomenon driven by electron beam charging and flexoelectricity (the coupling between strain gradient and polarization [17]). Lanthanide scandates, such as DyScO₃, are heavily distorted orthorhombic perovskites with space group *Pbnm* at room temperature and atmospheric pressure [18]. They have been extensively used as substrates for thin film oxide growth [19] and explored as potential gate oxide materials due to their high dielectric constants [20,21]. As was recently shown, lanthanide scandates charge considerably under very low flux

transmission electron microscope (TEM) beam illumination because their band gaps are approximately equal to their work functions, and when few defects are present, such as in well-annealed samples or hydrosol synthesized nanoparticles [22], there are minimal states available to trap secondary electrons. This was demonstrated with secondary electron imaging [16]. Therefore, any electrons with sufficient energy to be promoted to the conduction band instead exit the material, leaving behind a net positively charged sample. The charging is anisotropic, with the evidence indicating that the entrance surface and the side surface closest to the highest-flux region of the illumination are more positive than the exit surface and the side surface furthest from the highest-flux region of the illumination, which is intuitively expected. This unbalanced charging phenomenon coupled with an abnormally large flexocoupling voltage in DyScO₃ yields large reversible bending corresponding to strains which approach or exceed the nominal yield strength of typical, brittle ceramics, with the total potential difference across the sample limited by Zener tunneling [16].

This observation of flexoelectric bending, and the likely existence of other novel charging related phenomena, illustrates that charging is both good and bad. In some cases, it can be desirable (e.g. mechanical motion from charging for device applications [16]), whereas in other cases it must be avoided (e.g. electron cryomicroscopy [23]). It is also important to realize that in some materials, such as lanthanide scandates, charging cannot be avoided. In these situations, how does one

* Corresponding author.

E-mail address: L-marks@northwestern.edu (L.D. Marks).

<https://doi.org/10.1016/j.ultramic.2018.12.005>

Received 9 September 2018; Accepted 5 December 2018

Available online 06 December 2018

0304-3991/ © 2018 Elsevier B.V. All rights reserved.

probe electronic structure with TEM in a manner that yields meaningful results? Further, in charged materials do TEM results correlate with other experimental and theoretical tools?

In this paper, we provide an example of how to overcome charging effects on electron energy loss spectroscopy (EELS) to facilitate quantitative valence EELS analysis of a lanthanide scandate, DyScO₃. The results are combined with density functional theory (DFT) calculations which cross-validate the identification of an EELS peak below the bulk edge as a surface state. Further information about the physics of charging in DyScO₃ is provided by ultraviolet photoelectron spectroscopy (UPS) where well-annealed samples show evidence for Zener tunneling limited *negative* surface charging, correlating to the charging saturation limit previously observed [16].

2. Methods

A 3 mm disc was cut with an ultrasonic cutter from a commercially available single crystalline substrate (MTI Corp, Richmond, CA) of (110) oriented DyScO₃. This disc was then thinned to ~100 μm thick with silicon carbide sandpaper and dimpled with a Gatan 656 Dimple Grinder (0.5 μm diamond slurry) to ~15 μm thick at the center. Subsequently, the sample was Ar⁺ ion milled to electron transparency using a Gatan Precision Ion Polishing System (PIPS-I) starting at an energy of 5 keV and milling angle of 10°. The ion energy and milling angles were gradually brought down to 3 keV and 4°, respectively, for final polishing and surface cleaning. Lastly, the sample was annealed for 8–12 h in air at 1050–1200 °C in a tube furnace. Similar conditions have been used to prepare samples with surface reconstructions on other oxides, particularly SrTiO₃ and LaAlO₃ [24–28].

UPS data were acquired on a multisource ESCALAB 250Xi using a high photon flux ($> 1.5 \times 10^{12}$ photons/second) UV source with a spot size of ~1.5 mm. The source energy was 40.8 eV (He II). A pass energy of 10 eV was used with steps of 0.05 eV and 50 ms dwell time.

EELS data were acquired on a JEOL ARM200CF equipped with a cold field emission source and a CEOS probe spherical-aberration corrector. It was operated at 200 kV with a semi-convergence angle of 27 mrad. A Gatan Enfina EELS spectrometer was used with a dispersion of 0.05 eV/channel, collection angle of 22 mrad, and acquisition time of 1 μs (although in practice this is closer to 0.1 ms due to detector limitations). 100 individual spectra were acquired under constant illumination at these conditions and then analyzed as described below.

DFT calculations were performed with the all-electron augmented plane wave + local orbitals WIEN2K code [29]. Muffin tin radii of 1.68, 1.82, and 2.02 were used for O, Sc, and Dy, respectively, to minimize the inclusion of O2p tails within the metal muffin tins which perturbs the calculation of the exact-exchange corrections inside the muffin tins for Sc and Dy. The plane-wave expansion parameter RKMAX was 7.0. The electron density and (when appropriate) all atomic positions were simultaneously converged using a quasi-Newton algorithm [30]. Both an on-site hybrid approach [31,32] as well as a GGA + U approach using the PBEsol [33] functional were used. A slab model with a $70.000 \times 7.926 \times 7.936$ Å cell was used containing 260 atoms (92 unique) with P121/m1 symmetry, 18.3 Å of vacuum, and a $6 \times 6 \times 1$ k-mesh. A detailed comparison of bulk DFT calculations and valence x-ray photoelectron spectra for DyScO₃ has been previously described [34].

3. Results

Fig. 1(a) shows low-loss EELS data for DyScO₃ from a charged sample obtained with standard acquisition times. This spectrum was acquired by summing 100 individual spectra with no charging-correction obtained under the conditions given in the Methods section. Although some general features of the low-loss region were discernible, e.g. peak locations, this spectrum highlighted the adverse effects of sample charging: charging-related instabilities reduced the signal-to-

noise ratio (SNR) such that any quantitative analysis was near impossible. For example, the valence region was poorly defined and very noisy.

The cause of the low SNR can be understood by studying each individual spectrum in the summed spectrum in Fig. 1(a). An example of an individual spectrum is included in Fig. 1(b). As anticipated, this spectrum had a lower SNR than the summed spectrum in Fig. 1(a) because its acquisition time was effectively two orders of magnitude smaller. By studying all the individual spectra, it was apparent that interactions between the electron beam and charge on the sample induced energy loss shifts. This shift was quantified by tracking the zero-loss peak (ZLP) position in each individual spectrum. As shown in Fig. 1(c), the ZLP position wandered by as much as 2 eV over the course of the experiment. The average position of the ZLP in each spectrum tended to a steady-state value as the sample was further exposed to the beam, which we interpret as saturation of charging [16]. The fact that the average ZLP shift was positive indicates a positive charge developed on the sample (in agreement with previous work [16]). We note that although the average ZLP position evolved over the course of the experiment, the spread about the average value was consistently ~0.5 eV. This implies that while charging saturated on average, there were still local fluctuations in the charge distribution as the sample interacted with the beam.

Because the cause of the low SNR in the summed spectrum in Fig. 1(a) was the energy loss shift in each individual spectrum due to charging, one way to mitigate the effects of charging was to correct the origin in each individual spectrum prior to summing [35,36]. This was performed by choosing one spectrum as a reference and cross-correlating the other spectra with it. The results of this cross-correlation process are shown in Fig. 2(a) and (b) and demonstrate that the SNR and resolution were greatly improved by cross-correlating the ZLP position and correcting for charging shifts before the summation. We note that even if a sufficient number of spectra were acquired such that any transient effects are effectively averaged out, Fig. 1(c) demonstrates that ~0.5 eV fluctuations persist in the steady-state regime.

With this higher SNR spectrum, it was possible to study the valence and low-loss regions in greater detail. In the remainder of this paper, we focus on the valence region. The first test to determine the utility of the cross-correlated and summed spectra method was to extract the band gap. There are numerous methods to determine a band gap from EELS (e.g. [37]). We used a linear-fit method commonly used in the Auger electron spectroscopy and reflection EELS community in part due to its simplicity, and because it appears suitable for large band gap insulators [38]. The linear-fit method consists of finding the intersection between a line fit to the onset of the loss spectrum and a horizontal line at the background level. As shown in Fig. 2(c), this process yielded a minimum energy loss of ~5.4 eV. We are deliberately using “minimum energy loss” because evanescent states at the vacuum level (work function) as well as local states in the conduction band are possible in thin samples. This is close to previously reported experimental [16,39] and calculated [34,39] band gaps of 5.7 eV and 5.3 eV, respectively, as well as the experimental work function of 5.8 eV [16].

More involved methods of finding the band gap were thwarted by the presence of a feature at 3.8 eV, which we now turn to. First, it was important to determine if this was a real sample feature or an artifact because the existence of an in-gap state could provide insight into the charging dynamics of these heavily charging lanthanide scandates. We note that the Kimoto limit (the energy at which the intensity of the ZLP tail drops below $1e-3$ of the maximum ZLP intensity [40]), determined to be 3 eV, does not preclude this possibility. An interpretation of this feature was confounded by the typical difficulties associated with treating the ZLP and its long tail [35,41], so the approach adopted in this work was a Fourier-ratio deconvolution method using a Gaussian deconvolution function [35,41–43]. Because an experimentally acquired instrument response function was unavailable, the instrument response function was modeled with a number of functions (simple

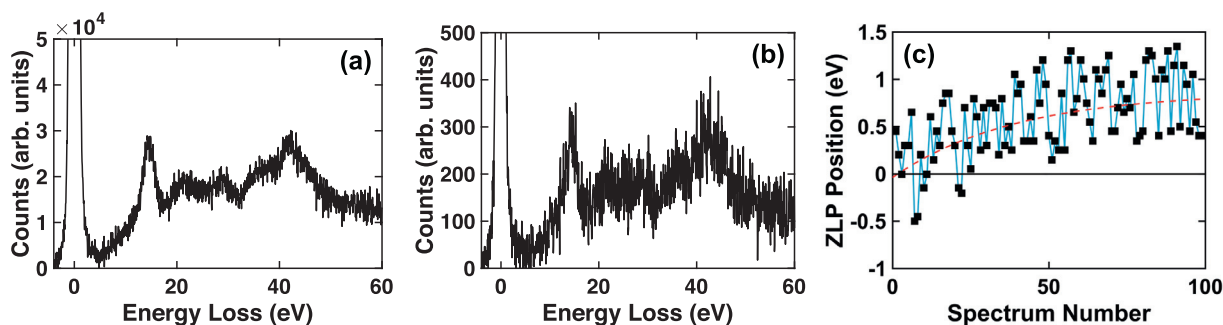


Fig. 1. Effects of charging on EELS data. (a) Energy loss spectrum of charged DyScO₃ obtained by summing 100 spectra each with an effective acquisition time of 0.1 ms and no charging-correction. Although some general features are identifiable, charging effects led to a low signal-to-noise ratio. (b) One of the individual spectra included in the sum used to obtain the spectrum in (a). (c) Zero-loss peak (ZLP) position of each 100 spectra shows energy loss shifts due to charging effects. The average ZLP position (red dashed line), and charging, tends to saturate. The constant spread in ZLP energy loss shifts around the average ZLP positions suggests local fluctuations in the charge distribution persist even after the charging has saturated on average. (For interpretation of color in this figure, the reader is referred to the web version of this article.)

truncations, power law, Gaussians, Gaussian-Lorentzian mixtures, Pearson VII) fit to the experimental ZLP shown in Fig. 2(a). An example of the results of the Fourier-ratio deconvolution is shown in Fig. 3. Although fitting to the ZLP is not the most robust method, the 3.8 eV feature persisted for every ZLP model used and for a wide range of Gaussian deconvolution full-width-half-maximum values. Therefore, the possibility that the 3.8 eV feature was an artifact was excluded.

We must now confront the possibility that the 3.8 eV feature was the result of a Cerenkov process: DyScO₃ has a high dielectric constant [21] and is firmly in the Cerenkov regime under the experimental conditions used here [44]. There are experimental methods to obtain energy loss spectra that minimize the collection of Cerenkov losses and simulations to determine Cerenkov loss energies [37,45]. We chose a different option: compare to DFT calculations. The surface of DyScO₃ contains a Sc-rich double-layer consisting of ScO₄ tetrahedra, ScO₅ octahedra with an unoccupied oxygen site, and ScO₆ octahedra as shown in Fig. 4(a) and (b) [16,46]. Since the Sc and O in the double-layer are in slightly different bonding environments than in bulk DyScO₃, there are localized electronic states and other deviations from bulk electronic structure as shown in Fig. 4(c)–(f). In particular, there are surface states with primarily Sc3d character below the bulk conduction band at ~ 3.7 eV above the valence band maximum (VBM). The location of this peak is consistent with the 3.8 eV loss peak seen in the charging-corrected energy loss spectrum which implies that this feature is not a Cerenkov loss. In addition, the 3.8 eV peak intensity is consistent with that of a surface state: estimating the sample thickness as 50 nm and the total surface thickness as 1.5 nm (2 surfaces), one would expect the surface energy loss features to be 3% of the intensity of the bulk energy loss

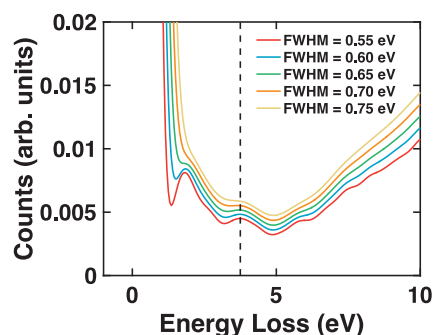


Fig. 3. Example of results of Fourier-ratio deconvolution analysis. This data demonstrates how the feature at 3.8 eV (black dashed line) is present independent of the full-width-half-maximum of the Gaussian deconvolution function when modeling the zero-loss peak (ZLP) as a Pearson VII function. Similar results were found using other ZLP models. Features below 3 eV fall below the Kimoto limit, but the peak at ~ 1.8 eV could be real as discussed later. (For interpretation of color in this figure, the reader is referred to the web version of this article.)

features. This is reasonably close to our findings

UPS is another experimental technique well-suited to study the electronic structure of surfaces [47]. Fig. 5(a) shows UPS data for well-annealed DyScO₃. With incident radiation of 40.8 eV and a work function of 5.8 eV the maximum kinetic energy of a photoelectron at the detector should be 35 eV, but in practice kinetic energies exceeding 45 eV were measured. This indicated the sample surface was negatively

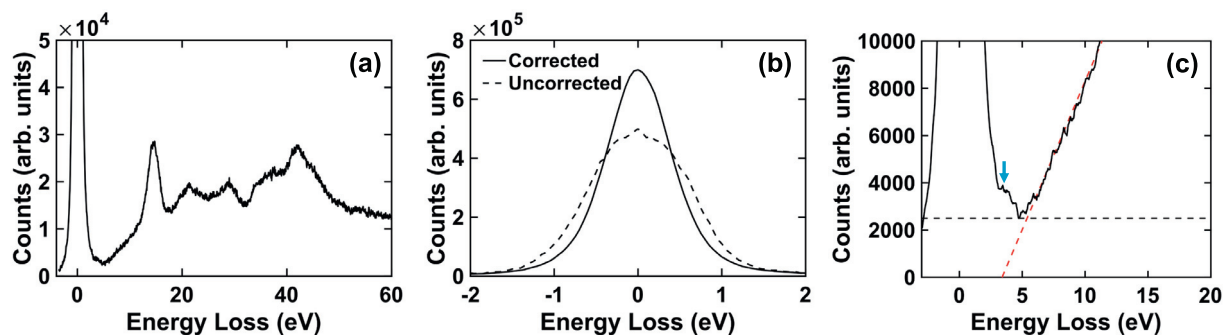


Fig. 2. Charging-corrected energy loss spectrum. (a) Energy loss spectrum shown in Fig. 1(a) after an origin correction using cross-correlation. This greatly enhanced the signal-to-noise ratio and interpretability of the data. For example, it is now apparent that there is an in-gap feature at approximately 3.8 eV, arrowed in (c). (b) After origin correction the full-width-half-maximum of the zero-loss peak was reduced by 0.5 eV. (c) The band gap of DyScO₃ was determined to be 5.4 eV using a linear-fit method with the spectrum in (a). The data were smoothed using a moving average of 5 data points prior to linear fitting. The linear fit marking the onset of the loss spectrum is a red dashed line and the background level is a black dashed line. (For interpretation of color in this figure, the reader is referred to the web version of this article.)

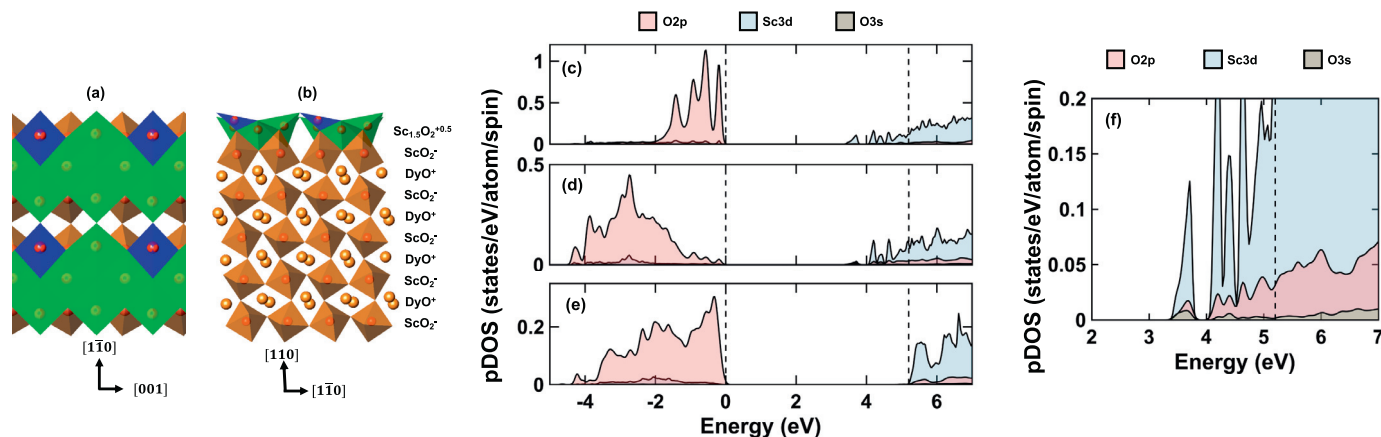


Fig. 4. Surface structure and density of states analysis of DyScO_3 . (a) and (b) show two different views of the DFT relaxed surface structure of DyScO_3 with 2.5 excess surface ScO_2 in a scandium-rich double layer: (a) from the top and (b) from the side. ScO_4 tetrahedra are in blue, ScO_5 octahedra with an unoccupied oxygen site are in green, and ScO_6 octahedra are in brown. The valence per formula unit of each layer shown in (b) is included on the right of the structure. (c) – (e) show the $\text{O}2p$, $\text{Sc}3d$, and $\text{O}3s$ partial density of states (pDOS) associated with this structure. (c), (d), and (e) correspond to the pDOS associated with the ScO_4 tetrahedra, ScO_5 octahedra with an unoccupied oxygen site, and bulk ScO_6 octahedra, respectively. In all cases, the valence band and conduction band are predominately $\text{O}2p$ and $\text{Sc}3d$ in character, respectively. The $\text{O}2p$ states from the ScO_4 tetrahedra have a centroid that is ~ 1 eV higher than the bulk $\text{O}2p$ states. (f) Unoccupied pDOS show that the surface states 3.7 eV above the valence band maximum (VBM) are mostly $\text{Sc}3d$ in character with some $\text{O}2p$ and $\text{O}3s$ contributions. In (c) – (f) the bulk band gap and VBM are shown with dashed black lines, and the VBM is taken to be 0 eV. (For interpretation of color in this figure, the reader is referred to the web version of this article.)

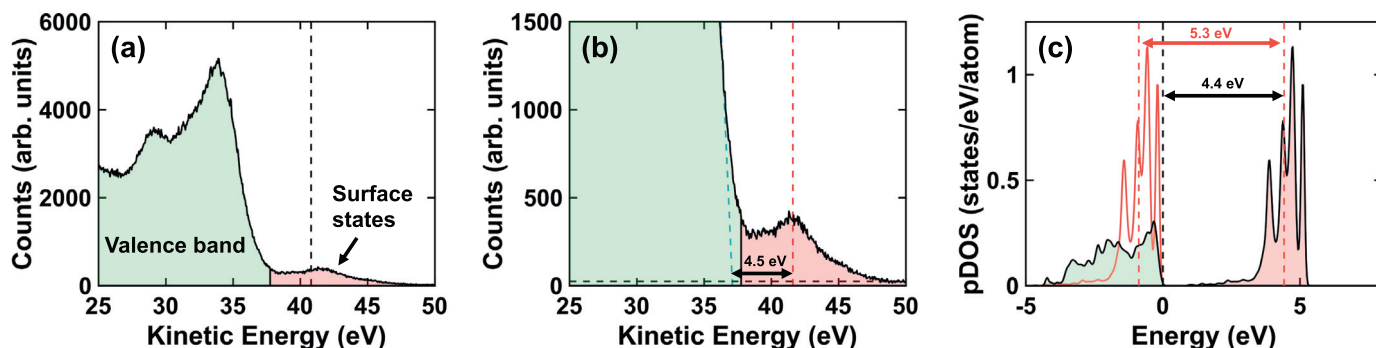


Fig. 5. Explanation of negative charging and in-gap state observed in UPS. (a) Ultraviolet photoelectron spectrum of DyScO_3 valence band reproduced from [34]. The black dashed line corresponds to incident ultraviolet light energy (40.8 eV). The measurement of photoelectrons with kinetic energies higher than this indicates negative charging. Features in green correspond to the valence band, which at these incident energies is dominated by $\text{O}2p$ states. Red corresponds to an in-gap feature. (b) The center of the in-gap feature is shown with a red dashed line. The green dashed line indicates a linear extrapolation of the valence band maximum (VBM). The difference between where the two lines intersect the background level (black dashed line) is ~ 4.5 eV. (c) Partial occupied density of states of bulk (green) and surface (red) $\text{O}2p$ states. After negative charging has saturated, the maximum shift in the surface states is the band gap (red dashed lines) which centers the surface states ~ 4.4 eV above the VBM (black dashed line). (For interpretation of color in this figure, the reader is referred to the web version of this article.)

charged, similar to what can occur in low-voltage scanning electron microscopy. We argue this is because secondary electrons produced in the bulk (the UV penetration depth is much larger than the secondary electron escape depth) accumulate at the surface leading to a net negative surface charge (and a net positive charge in the sub-surface region). An accumulation of negative charge at the surface would cause occupied surface electronic states (in this case $\text{O}2p$ states) to bend up. Therefore, we interpret the 29.1 eV and 33.8 eV features as bulk states and the 41.6 eV feature as the bent $\text{O}2p$ surface states. The maximum band bending, i.e. the maximum potential difference, is set by the band gap because any additional band bending will induce Zener tunneling [48]. This suggests that if Zener tunneling is the limiting factor, then the bent $\text{O}2p$ surface states should be centered ~ 4.5 eV above the VBM because the centroid of the $\text{O}2p$ surface states is ~ 1 eV below the VBM as shown in Fig. 5(c). This is in good agreement with the UPS results and supports the Zener tunneling limit for the potential difference that can be achieved [16]. The long tails at higher kinetic energies above this peak are consistent with fluctuations in the charging, which were also observed in the EELS results as mentioned before.

4. Discussion

There is rich physics in charging of samples inside electron microscopes involving information about local electronic states, band bending as well as higher order electromechanical couplings such as the flexoelectric effect. Exactly what will be present in a sample is a strong function of the number and density of local states as well as surface structure. Most experimental samples in electron microscopy have relatively poorly defined surfaces, contamination or damaged layers, and unintentional concentrations of point defects. If these are avoided we believe there is significant new science that can be explored, albeit not the easiest electron microscopy as samples tend to be very unstable.

One issue we have not addressed in detail here is the not-well-defined possible peak in the EELS data at ~ 1.8 eV. Although this is below the Kimoto limit and it could be due to Cerenkov radiation, it is worth discussing some other possible origins of this feature because the samples are positively charged in TEM and a 1.8 eV loss could be a result of charging induced changes to the electronic structure. One would expect the charge to be longest lived in states near the Fermi

level, which would be the O2p states at the surface and minority Dy4f states in the bulk [34]. Since the centroid of the surface O2p states is ~ 1 eV higher than the centroid of the bulk O2p states, charge transfer between the bulk and surface O2p states is possible. Another possibility is the existence of local Dy⁴⁺ states. The loss of an additional electron in the localized 4f states will pull the unoccupied minority 4f states down in energy, which could lead to available states close to the VBM. There is some exploration of Dy⁴⁺ defects in the literature [49,50], but as of yet there is no definitive analysis. Unfortunately, performing reasonably accurate calculations to model these hypotheses are at, or beyond, the current state-of-the-art for DFT which is really a ground state calculation. One can partially model core-hole relaxation using a Hubbard U as we previously demonstrated [34], but this is not a complete solution.

One final comment is worth making; understanding some of the complex phenomena associated with charging and potential gradients across samples may have wider relevance. As mentioned earlier there are clear indications of bending and charging in electron cryomicroscopy [6,12]. While research on the flexoelectric effect in bulk ceramics is relatively new [17], flexoelectricity in biological systems, such as membranes [51], has been shown to be of some importance for physiological function [52,53]. It is quite possible that bending of electron cryomicroscopy samples could be exploited to measure physiologically relevant electromechanical couplings, for instance by depositing electrodes on samples, however we will leave this speculation to the future.

5. Conclusion

Charging is a ubiquitous phenomenon in electron microscopy. Although it is typically avoided, its effects should not always be discounted as artifacts because charging can be a source of new science. Moreover, charging is unavoidable in some materials, and in these cases it is still important to be able to utilize an electron microscope to answer relevant questions in spite of charging effects. In this paper, we used a combination of rapidly acquired energy loss spectra and cross-correlation to overcome charging effects. This allowed for the extraction of an accurate band gap and, with complementary DFT, the attribution of an in-gap feature to surface states. Additionally, UPS results demonstrated Zener tunneling limiting potential differences is also relevant for negatively charged samples.

Acknowledgments

This work was supported by the U.S. Department of Energy, Office of Science, Basic Energy Sciences, under Award # DE-FG02-01ER45945. Electron microscopy was performed at the UIC Research Resources Center supported by an MRI-R² grant from the National Science Foundation (NSF DMR-0959470).

References

- J. Cazaux, Some considerations on the electric field induced in insulators by electron bombardment, *J. Appl. Phys.* 59 (1986) 1418–1430.
- D.B. Dove, Image contrasts in thin carbon films observed by shadow electron microscopy, *J. Appl. Phys.* 35 (1963) 1652.
- J. Cazaux, Correlations between ionization radiation damage and charging effects in transmission electron microscopy, *Ultramicroscopy* 60 (1995) 411–425.
- J.W. Chen, G. Matteucci, A. Migliori, G.F. Missiroli, E. Nichelatti, G. Pozzi, M. Vanzì, Mapping of microelectrostatic fields by means of electron holography: theoretical and experimental results, *Phys. Rev. A* 40 (1989) 3136–3146.
- R.F. Egerton, P. Li, M. Malac, Radiation damage in the TEM and SEM, *Micron* 35 (2004) 399–409.
- R.M. Glaeser, K.H. Downing, Specimen charging on thin films with one conducting layer: discussion of physical principles, *Microsc. Microanal.* 10 (2004) 790–796.
- P.F. Fazzini, P.G. Merli, G. Pozzi, F. Ubaldi, Effects of beam-specimen interaction on the observation of reverse-biased p–n junctions by electron interferometry, *Phys. Rev. B* 72 (2005) 085312.
- M.R. McCartney, Characterization of charging in semiconductor device materials by electron holography, *J. Electron Microsc.* 54 (2005) 239–242.
- M. Beleggia, T. Kasama, R.E. Dunin-Borkowski, S. Hofmann, G. Pozzi, Direct measurement of the charge distribution along a biased carbon nanotube bundle using electron holography, *Appl. Phys. Lett.* 98 (2011) 243101.
- E.R. White, M. Mecklenburg, B. Shevitski, S.B. Singer, B.C. Regan, Charged nanoparticle dynamics in water induced by scanning transmission electron microscopy, *Langmuir* 28 (2012) 3695–3698.
- C. Gatel, A. Lubk, G. Pozzi, E. Snoeck, M. Hÿtch, Counting elementary charges on nanoparticles by electron holography, *Phys. Rev. Lett.* 111 (2013) 025501.
- C.J. Russo, R. Henderson, Charge accumulation in electron cryomicroscopy, *Ultramicroscopy* 187 (2018) 43–49.
- J. Brink, M.B. Sherman, J. Berriman, W. Chiu, Evaluation of charging on macromolecules in electron cryomicroscopy, *Ultramicroscopy* 72 (1998) 41–52.
- U. Jakubowski, W. Baumeister, R.M. Glaeser, Evaporated carbon stabilizes thin, frozen-hydrated specimens, *Ultramicroscopy* 31 (1989) 351–356.
- C.J. Russo, L.A. Passmore, Ultrastable gold substrates: properties of a support for high-resolution electron cryomicroscopy of biological specimens, *J. Struct. Biol.* 193 (2016) 33–44.
- P. Koirala, C.A. Mizzi, L.D. Marks, Direct observation of large flexoelectric bending at the nanoscale in lanthanide scandates, *Nano Lett.* 18 (2018) 3850–3856.
- P. Zubko, G. Catalan, A.K. Tagantsev, Flexoelectric effect in solids, *Ann. Rev. Mater. Res.* 43 (2013) 387–421.
- M. Schmidbauer, A. Kwasniewski, J. Schwarzkopf, High-precision absolute lattice parameter determination of SrTiO₃, DyScO₃ and NdGaO₃ single crystals, *Acta Crystallogr. B* 68 (2012) 8–14.
- J.H. Haeni, P. Irvin, W. Chang, R. Uecker, P. Reiche, Y.L. Li, S. Choudhury, W. Tian, M.E. Hawley, B. Craigo, A.K. Tagantsev, X.Q. Pan, S.K. Streiffer, L.Q. Chen, S.W. Kirchoefer, J. Levy, D.G. Schlom, Room-temperature ferroelectricity in strained SrTiO₃, *Nature* 430 (2004) 758–761.
- V.V. Afanas'ev, A. Stesmans, C. Zhao, M. Caymax, T. Heeg, J. Schubert, Y. Jia, D.G. Schlom, G. Lucovsky, Band alignment between (100)Si and complex rare earth/transition metal oxides, *Appl. Phys. Lett.* 85 (2004) 5917–5919.
- S. Coh, T. Heeg, J.H. Haeni, M.D. Biegalski, J. Lettieri, L.F. Edge, K.E. O'Brien, M. Bernhagen, P. Reiche, R. Uecker, S. Trolier-McKinstry, D.G. Schlom, D. Vanderbilt, Si-compatible candidates for high-κ dielectrics with the Pbnm perovskite structure, *Phys. Rev. B* 82 (2010) 064101.
- R.J. Paull, Z.R. Mansley, T. Ly, L.D. Marks, K.R. Poeppelmeier, Synthesis of gadolinium scandate from a hydroxide hydrogel, *Inorg. Chem.* 57 (2018) 4104–4108.
- K.H. Downing, M.R. McCartney, R.M. Glaeser, Experimental characterization and mitigation of specimen charging on thin films with one conducting layer, *Microsc. Microanal.* 10 (2004) 783–789.
- N. Erdman, L.D. Marks, SrTiO₃(001) surface structures under oxidizing conditions, *Surf. Sci.* 526 (2003) 107–114.
- N. Erdman, K.R. Poeppelmeier, M. Asta, O. Warschkow, D.E. Ellis, L.D. Marks, The structure and chemistry of the TiO₂-rich surface of SrTiO₃ (001), *Nature* 419 (2002) 55–58.
- N. Erdman, O. Warschkow, M. Asta, K.R. Poeppelmeier, D.E. Ellis, L.D. Marks, Surface structures of SrTiO₃ (001): a TiO₂-rich reconstruction with a c(4 × 2) unit cell, *J. Am. Chem. Soc.* 125 (2003) 10050–10056.
- D.M. Kienzie, A.E. Becerra-Toledo, L.D. Marks, Vacant-site octahedral tilings on SrTiO₃(001), the (13 × 13)R33.7° surface, and related structures, *Phys. Rev. Lett.* 106 (2011) 176102.
- P. Koirala, E. Steele, A. Gulec, L.D. Marks, Al rich (111) and (110) surfaces of LaAlO₃, *Surf. Sci.* 677 (2018) 99–104.
- P. Blaha, K. Schwarz, G.K.H. Madsen, D. Kvasnicka, J. Luitz, R. Laskowski, F. Tran, L.D. Marks, An Augmented Plane Wave + Local Orbitals Program For Calculating Crystal Properties, Techn. Universitat Wien, Austria, 2018.
- L.D. Marks, Fixed-point optimization of atoms and density in DFT, *J. Chem. Theory Comput.* 9 (2013) 2786–2800.
- P. Novak, J. Kunes, L. Chaput, W.E. Pickett, Exact exchange for correlated electrons, *Phys. Status Solidi B* 243 (2006) 563–572.
- F. Tran, J. Kunes, P. Novak, P. Blaha, L.D. Marks, K. Schwarz, Force calculation for orbital-dependent potentials with FP-(L)APW plus lo basis sets, *Comput. Phys. Commun.* 179 (2008) 784–790.
- J.P. Perdew, A. Ruzsinszky, G.I. Csonka, O.A. Vydrov, G.E. Scuseria, L.A. Constantin, X. Zhou, K. Burke, Restoring the density-gradient expansion for exchange in solids and surfaces, *Phys. Rev. Lett.* 100 (2008) 136406.
- C.A. Mizzi, P. Koirala, L.D. Marks, Electronic structure of lanthanide scandates, *Phys. Rev. Mater.* 2 (2018) 025001.
- B. Rafferty, S.J. Pennycook, L.M. Brown, Zero loss peak deconvolution for bandgap EEL spectra, *J. Electron Microsc.* 49 (2000) 517–524.
- Y. Sasano, S. Muto, Energy-drift correction of electron energy-loss spectra from prolonged data accumulation of low SNR signals, *J. Electron Microsc.* 57 (2008) 149–158.
- M. Stöger-Pollach, Optical properties and bandgaps from low loss EELS: pitfalls and solutions, *Micron* 39 (2008) 1092–1110.
- J. Park, S. Heo, J.G. Chung, H. Kim, H. Lee, K. Kim, G.S. Park, Bandgap measurement of thin dielectric films using monochromated STEM-EELS, *Ultramicroscopy* 109 (2009) 1183–1188.
- C. Derks, K. Kuepper, M. Raekers, A.V. Postnikov, R. Uecker, W.L. Yang, M. Neumann, Band-gap variation in RScO₃ (R = Pr, Nd, Sm, Eu, Gd, Tb, and Dy): X-ray absorption and O K-edge x-ray emission spectroscopies, *Phys. Rev. B* 86 (2012) 155124.
- K. Kimoto, G. Kothleitner, W. Grogger, Y. Matsui, F. Hofer, Advantages of a monochromator for bandgap measurements using electron energy-loss spectroscopy, *Micron* 36 (2005) 185–189.
- R.F. Egerton, *Electron Energy-Loss Spectroscopy in the Electron Microscope*, 2 ed., Plenum, New York, 1996.

- [42] J.A. Aguiar, B.W. Reed, Q.M. Ramasse, R. Erni, N.D. Browning, Quantifying the low-energy limit and spectral resolution in valence electron energy loss spectroscopy, *Ultramicroscopy* 124 (2013) 130–138.
- [43] F. Wang, R.F. Egerton, M. Malac, Fourier-ratio deconvolution techniques for electron energy-loss spectroscopy (EELS), *Ultramicroscopy* 109 (2009) 1245–1249.
- [44] M. Stöger-Pollach, H. Franco, P. Schattschneider, S. Lazar, B. Schaffer, W. Grogger, H.W. Zandbergen, Cerenkov losses: A limit for bandgap determination and Kramers–Kronig analysis, *Micron* 37 (2006) 396–402.
- [45] M. Stöger-Pollach, P. Schattschneider, The influence of relativistic energy losses on bandgap determination using valence EELS, *Ultramicroscopy* 107 (2007) 1178–1185.
- [46] C.A. Mizzi, Z.R. Mansley, P. Koirala, L.D. Marks, Sc-rich (110) surfaces of DyScO₃, GdScO₃, and TbScO₃ single crystals, In preparation.
- [47] S. Hüfner, *Photoelectron Spectroscopy: Principles and Applications*, Springer, Berlin, 2003.
- [48] C. Zener, A theory of the electrical breakdown of solid dielectrics, *Proc. R. Soc. A* 145 (1934) 523–529.
- [49] R. Uecker, B. Velickov, D. Klimm, R. Bertram, M. Bernhagen, M. Rabe, M. Albrecht, R. Fornari, D.G. Schlom, Properties of rare-earth scandate single crystals ($Re = \text{Nd-Dy}$), *J. Cryst. Growth* 310 (2008) 2649–2658.
- [50] B. Velickov, V. Kahlenberg, R. Bertram, M. Bernhagen, Crystal chemistry of GdScO₃, DyScO₃, SmScO₃ and NdScO₃, *Zeitschrift für Kristallographie – Cryst. Mater.* 222 (2007) 466–473.
- [51] A.G. Petrov, Flexoelectricity of model and living membranes, *Biochim. et Biophys. Acta* 1561 (2002) 1–25.
- [52] F. Vaquez-Sancho, A. Abdollahi, D. Damjanovic, G. Catalan, Flexoelectricity in bones, *Adv. Mater.* 30 (2018) 1705316.
- [53] K.D. Breneman, W.E. Brownell, R.D. Rabbitt, Hair cell bundles: flexoelectric motors of the inner ear, *PLoS One* 4 (2009) e5201.